nature physics

REVIEW ARTICLE

https://doi.org/10.1038/s41567-018-0051-x

Antiferromagnetic opto-spintronics

P. Němec[1]*, M. Fiebig[2], T. Kampfrath[3,4] and A. V. Kimel[5,6]

Control and detection of spin order in ferromagnetic materials is the main principle enabling magnetic information to be stored and read in current technologies. Antiferromagnetic materials, on the other hand, are far less utilized, despite having some appealing features. For instance, the absence of net magnetization and stray fields eliminates crosstalk between neighbouring devices, and the absence of a primary macroscopic magnetization makes spin manipulation in antiferromagnets inherently faster than in ferromagnets. However, control of spins in antiferromagnets requires exceedingly high magnetic fields, and antiferromagnetic order cannot be detected with conventional magnetometry. Here we provide an overview and illustrative examples of how electromagnetic radiation can be used for probing and modification of the magnetic order in antiferromagnets. We also discuss possible research directions that are anticipated to be among the main topics defining the future of this rapidly developing field.

Antiferromagnets (AFs) are materials in which magnetic moments are spontaneously long-range ordered, but with a net magnetic moment that is zero or small compared to the sum of participating magnetic moments[1]. AFs are considerably more common than ferromagnets (FMs). In particular, unlike FMs, they are permitted in each magnetic symmetry group. They can be insulators, metals, semimetals, semiconductors or superconductors, whereas FMs are predominantly metals. AFs also offer much greater structural flexibility than FMs because there are a large number of ways in which magnetic moments can be arranged to achieve a zero net moment (see Fig. 1a).

AFs exhibit a variety of unique functionalities of either intrinsic or engineered nature. On the intrinsic side, antiferromagnetism may be linked to a small secondary magnetization or polarization. In materials called 'canted AFs' or 'weak FMs', the magnetization can result from an antisymmetric form of exchange coupling termed Dzyaloshinskii–Moriya interaction[2,3], which results in a canting of two collinear antiferromagnetic spin-sublattices by about 1°. If the antiferromagnetic order breaks inversion symmetry, spin–spin interactions may give rise to an electric polarization of about 1–100 nC cm^{-2}. The simultaneous presence of antiferromagnetic and ferroelectric order makes the material a multiferroic[4,5]. On the engineering side, the so-called 'synthetic AFs' form materials with antiferromagnetically coupled layers of FMs (for more details, see the Perspective by Duine and colleagues[6] in this Focus issue). AFs are also frequently used as a reference layer in spin valves that fixes the magnetization orientation in FMs due to the exchange bias[7].

However, the potential of AFs is significantly larger, as envisioned in the concept of antiferromagnetic spintronics[8–13]. In particular, antiparallel spin sublattices in AFs, which produce zero dipolar fields, imply the insensitivity to magnetic-field perturbations[14,15] and multi-level stability[16,17] in magnetic memories. Another appealing property of AFs is the orders-of-magnitude faster spin dynamics than in FMs[18]. The frequency of uniform spin precession (antiferromagnetic resonance) is in the terahertz range due to strong exchange interaction between the spin sublattices[19–21], whereas ferromagnetic resonance due to the weaker anisotropy field is in the gigahertz frequency range[18,21]. However, the absence of a net magnetic moment, the frequently observed small size of magnetic domains and the ultrafast magnetization dynamics make probing of antiferromagnetic order by common magnetometers or magnetic resonance techniques notoriously difficult.

Light or, more generally, electromagnetic radiation is an invaluable tool for magnetic order probing. Methods enabling optical access to ferromagnetic order have been developed for over 150 years[22]. However, due to the absence of magnetization, antiferromagnetism is much harder to study by optical techniques. The respective approaches are quite young and still under development. The next section of this Review is devoted to a survey of the available techniques in the optical range and beyond (see Fig. 1).

Manipulation of magnetic order in AFs is the second challenge. The strength of an external magnetic field required to reorient spins in AFs scales with the exchange interaction and thus can exceed 100 T. Remarkably, light was shown to be an efficient tool to control spins[18,23]. Some of the mechanisms, such as inertia-driven spin switching[24], least dissipative impulsive excitation of spins[25], excitation of terahertz nanomagnons at the edge of the Brillouin zone[26] and reducing the spin noise below the standard quantum limit[27], have so far been demonstrated only in AFs or are even possible exclusively in these materials. Two sections of this Review will give an overview on antiferromagnetic order manipulation by light.

Detection techniques

Several detection techniques exist for probing antiferromagnetic order in bulk crystals, among which neutron diffraction plays the major role. However, for thin epitaxial films, which form the building blocks of devices, and for ultrafast transient processes or spatially resolved detection, this technique is usually not applicable. Below, we describe three distinct groups of detection techniques based on the interaction of electromagnetic radiation with AFs (see Fig. 1c): linear optical studies, nonlinear optical studies and terahertz emission and transmission spectroscopy.

Magneto-optics is an efficient probe of magnetic order[22,28] with high spatial[29] and temporal[18] resolution. Assuming that an AF has two equivalent magnetic sublattices represented by magnetizations $\mathbf{M}_1$ and $\mathbf{M}_2$, we can define two orthogonal vectors of magnetization $\mathbf{M} = \mathbf{M}_1 + \mathbf{M}_2$ and antiferromagnetism $\mathbf{L} = \mathbf{M}_1 - \mathbf{M}_2$ (see Fig. 1a). Linear optical properties are described by the dielectric permittivity tensor ε_{ij}, which can be written as a sum of the antisymmetric and symmetric parts $\varepsilon_{ij} = \varepsilon^{(a)}{}_{ij} + \varepsilon^{(s)}{}_{ij}$, where $\varepsilon^{(a)}{}_{ij} = -\varepsilon^{(a)}{}_{ji}$ and $\varepsilon^{(s)}{}_{ij} = \varepsilon^{(s)}{}_{ji}$. According to the Onsager principle, $\varepsilon^{(a)}{}_{ij}$ can only be an odd function with respect to $\mathbf{L}$, $\mathbf{M}$ and their combinations, while the dependence of $\varepsilon^{(s)}{}_{ij}$ on the order parameters is even[30].

[1]Faculty of Mathematics and Physics, Charles University, Prague, Czech Republic. [2]Department of Materials, ETH Zurich, Zurich, Switzerland. [3]Department of Physical Chemistry, Fritz Haber Institute of the Max Planck Society, Berlin, Germany. [4]Department of Physics, Freie Universität Berlin, Berlin, Germany. [5]Radboud University, Institute for Molecules and Materials, Nijmegen, the Netherlands. [6]Moscow Technological University, MIREA, Moscow, Russia. *e-mail: nemec@karlov.mff.cuni.cz

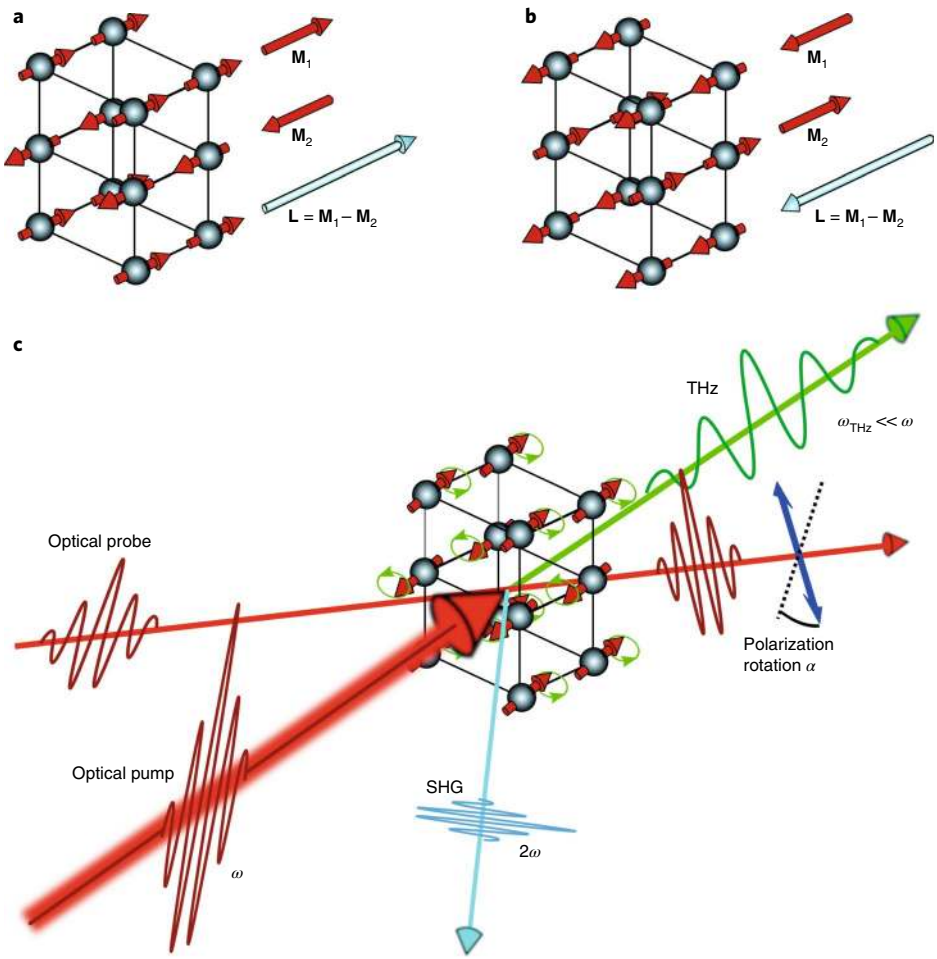

Fig. 1 | Schematics of investigation of antiferromagnets by electromagnetic radiation. Although AFs possess no net magnetization to couple to, there are numerous ways to observe their spin pattern. **a**, An example of an antiferromagnetic spin structure consisting of two oppositely aligned ferromagnetic planes. (Other examples of antiferromagnetic ordering are depicted in Figs. 5d and 8f.) $\mathbf{M}_1$ and $\mathbf{M}_2$ represent magnetization orientations in two magnetic sublattices from which the antiferromagnetic vector $\mathbf{L} = \mathbf{M}_1 - \mathbf{M}_2$ and the ferromagnetic vector $\mathbf{M} = \mathbf{M}_1 - \mathbf{M}_2 \approx 0$ can be defined. **b**, The opposite domain state of the same structure. **c**, An intense optical pump laser pulse, typically in the red or infrared spectral regions, brings the AF out of equilibrium, which can be measured by detecting the polarization rotation of a weaker optical probe pulse. Alternatively, magnetization-assisted SHG or electromagnetic radiation emitted by precessing spins in the terahertz spectral range can be used to monitor the dynamic and/or static properties of AFs.

Many magneto-optical (MO) studies have been performed in canted AFs[24,31–37], where the probe of antiferromagnetism relies on a linear dependence of $\varepsilon^{(a)}_{ij}$ on the secondary magnetization $\mathbf{M}$. A large MO Kerr effect was predicted also for the non-collinear AFs Mn_3X where X = Rh, Ir, Pt (ref. [38]). Assume a coordinate system with x and y axes in the sample plane and the z axis along the sample normal, where $\mathbf{M}$ is oriented. If, in the otherwise isotropic medium with relative dielectric permittivity ε, an external stimulus induces $\varepsilon^{(a)}_{xy}$, it will break the degeneracy between right- and left-handed circularly polarized light propagating in the z direction. Light of opposite helicity will be refracted and absorbed differently, resulting in circular birefringence and dichroism, respectively[39]. Linearly polarized light propagating along the z axis will experience a polarization rotation by an angle

$$\alpha_F = \frac{\omega\, d}{2c\sqrt{\mathrm{Re}(\varepsilon)}}\mathrm{Im}(\varepsilon^{(a)}_{ij}) \quad (1)$$

where ω is the light wave frequency, d is the sample length and c is the vacuum speed of light. Magnetization-induced polarization rotation (and ellipticity) upon transmission or reflection is called the MO Faraday and Kerr effect, respectively (see Fig. 1c). Even if the equilibrium magnetization is zero and no magnetic field is applied, the magnetization in AFs can still be induced[40] by coherent dynamics of spins $\mathbf{M} \sim \mathbf{L} \times \mathrm{d}\mathbf{L}/\mathrm{d}t$. Therefore, the dynamic magnetization can be used to probe pump-induced changes of the spin ordering in AFs[19,20,41].

An alternative MO approach is to use $\varepsilon^{(s)}_{ij}$, which depends quadratically on $\mathbf{L}$ and is, therefore, present even in compensated AFs (where M = 0). If, in an otherwise isotropic medium, the spins are antiferromagnetically ordered along the x axis, the alignment will change $\varepsilon^{(s)}_{ij}$, so that $\varepsilon^{(s)}_{xx} \neq \varepsilon^{(s)}_{yy}$, inducing linear dichroism and birefringence[18,22,28,29,42–44]. The former, which is usually called the Voigt or Cotton–Mouton effect, can be measured as a polarization rotation[45]. Contrary to the Faraday effect, the polarization rotation angle α_V is the largest when the light propagation direction is perpendicular to the spin orientation. It also depends on the angle between the incoming light polarization (β) and the $\mathbf{L}$ orientation (φ) according to

$$\alpha_V(\beta) = P^{\mathrm{MLD}} sin(2(\varphi - \beta)) \quad (2)$$

The MO coefficient P^{MLD}, which scales quadratically with the $\mathbf{L}$ projection onto the plane perpendicular to the light propagation

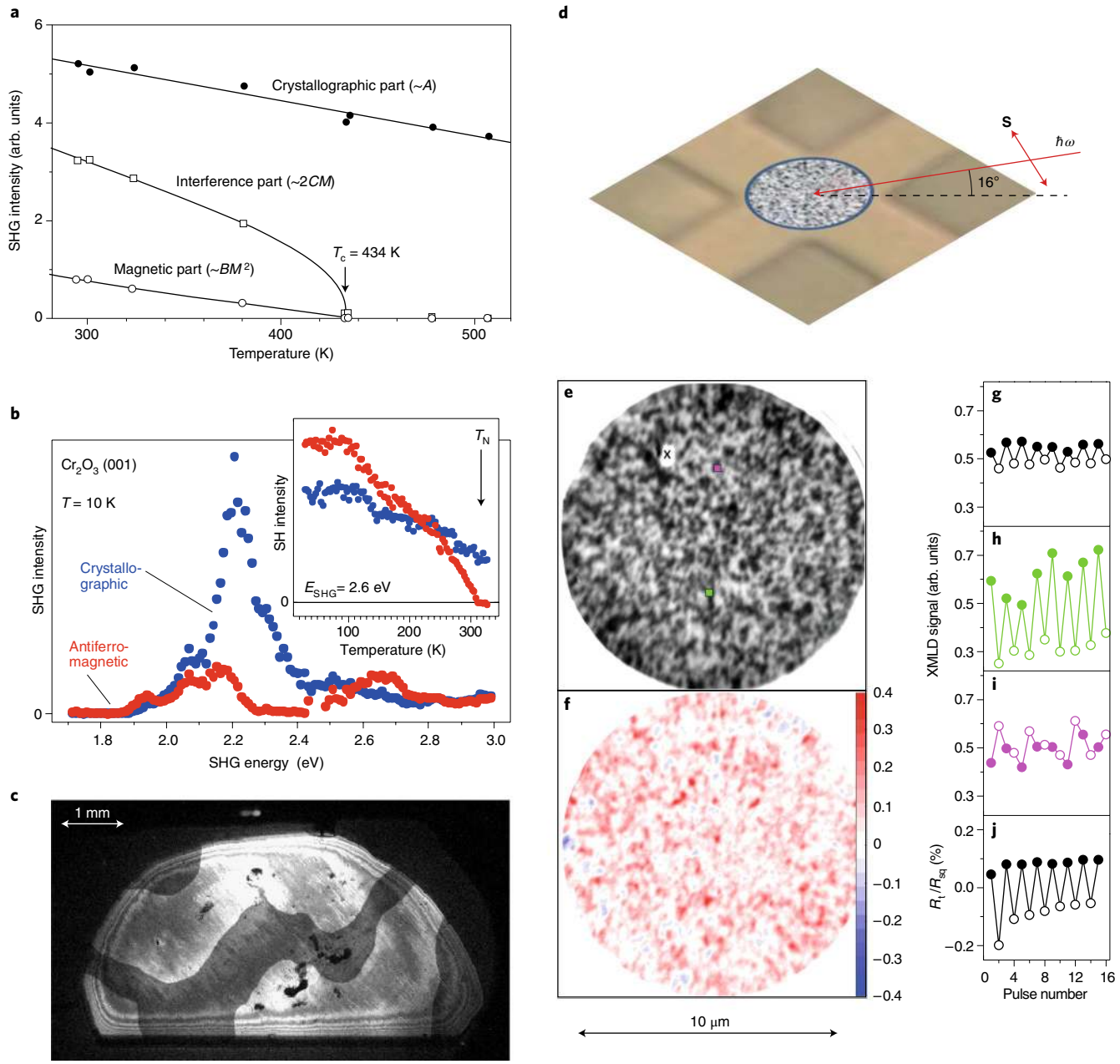

Fig. 2 | Visualization of antiferromagnetic domains by SHG and XMLD–PEEM. a, Temperature variation of crystallographic, magnetization-induced and interference terms of the SHG intensity of the Bi-YIG/GGG(111) film. **b**, SHG spectrum of a *z*-oriented Cr_2O_3 platelet. Light polarizations are chosen such that the crystallographic and antiferromagnetic SHG contributions are separated and measured background-free. The inset shows that the antiferromagnetic contribution vanishes at the Néel temperature whereas the crystallographic contribution remains[64]. **c**, SHG image of antiferromagnetic 180° domains on the Cr_2O_3 sample. By interference of the crystallographic and antiferromagnetic SHG contributions, opposite domain states exhibit a different degree of brightness[71,72]. **d**, Geometry of XMLD–PEEM measurements of a device made from CuMnAs. X-rays are incident at 16° to the surface, with the polarization vector **s** in the film plane. **e**, XMLD–PEEM image of the central section of the device. **f**, Difference between XMLD–PEEM images taken after applying trains of alternate orthogonal current pulses of 6.1 MA cm^{-2}. **g**, Spatially averaged XMLD signal after each pulse train. Open and filled symbols represent the two orthogonal pulse directions. **h**,**i**, As for **g**, but for the 200 × 200 nm^2 regions marked by green and pink squares in **e**, respectively. **j**, Change in the transverse resistance following the same pulse sequence. Credit: reproduced from ref. [71], OSA (**a**); and ref. [61], APS (**d**–**j**).

direction[45], is connected with magnetic linear dichroism (MLD): $P^{MLD} = 0.5(T_{||}/T_{\perp} - 1)$, where $T_{||}$ and $T_{\perp}$ are amplitude transmission coefficients for light polarized parallel and perpendicular to **L**, respectively[43,45]. Experimentally, the quadratic dependence on **L** and the low sensitivity of AFs to external magnetic fields significantly complicate the separation of the magnetic-order-related signal from linear dichroism and birefringence of other origins (for example, strain- or crystal-structure-related)[46]. This problem can be circumvented if a two-beam pump–probe experiment is used that utilizes the pump-induced reduction of **L**. For AFs, the quadratic MO effects were used for pump-induced dynamics detection both in weakly absorbing insulators[19,25,26,31,36,41] and in metals[45].

The quadratic dependence of $\varepsilon^{(s)}_{ij}$ on **L** results also in the polarization-independent phenomena of magneto-refraction and

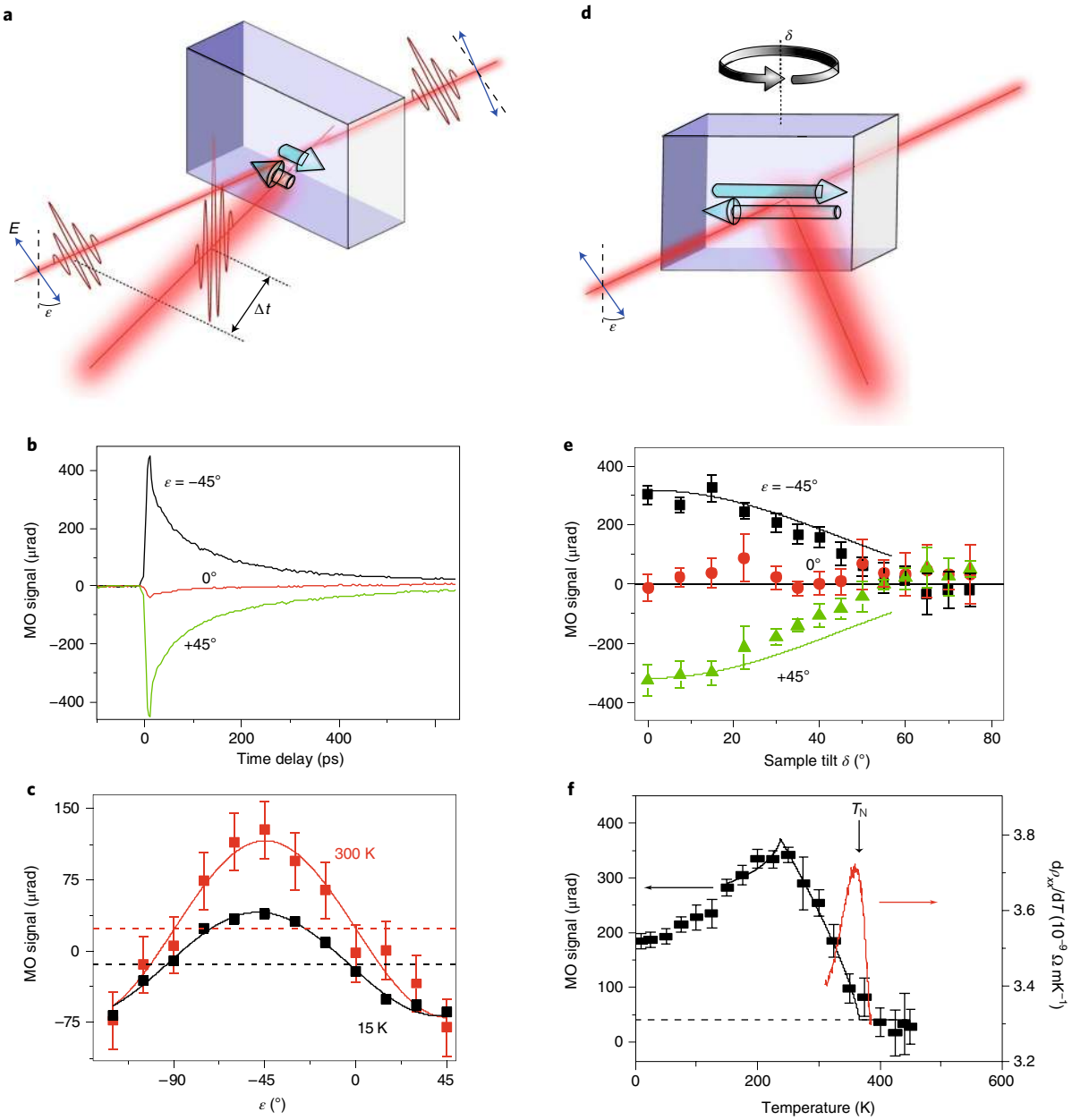

Fig. 3 | Determination of the uniaxial magnetic anisotropy direction and Néel temperature from pump-induced demagnetization in CuMnAs film. **a**, Schematic illustration of the pump-induced reduction of a light polarization plane rotation due to the Voigt effect. **b**, Pump-induced change of MO signal measured for various probe polarization orientations, ε, as a function of time delay, Δt, between pump and probe pulses. **c**, Probe-polarization dependence of MO signal measured for $\Delta t = 60$ ps at 15 K (black points) and 300 K (red points) for a 10-nm-thick CuMnAs film. Solid lines are fits by equation (2) plus polarization-independent backgrounds (dashed horizontal lines). **d**, Schematic illustration of sample tilting around an axis perpendicular to the direction of the magnetic moments, which is along the [110] substrate direction, leading to a reduction of the moment projection onto the plane perpendicular to the probe light propagation direction. **e**, MO signal measured for $\Delta t = 60$ ps (points) as a function of the sample tilt around the $[1\bar{1}0]$ substrate direction at 300 K. The solid lines depict the function $\cos^2\delta$ describing the moment projection reduction expected for the situation shown in **d**. **f**, Temperature dependence of MO signal (points) and sample resistivity temperature derivative (red line). The vertical arrow indicates the Néel temperature T_N. Credit: reproduced from ref. [45], Macmillan Publishers Ltd.

magneto-absorption. The effects were observed as an intensity change of diffracted X-rays in $La_{0.5}Sr_{1.5}MnO_4$ (ref. [47]), transmitted or reflected light in EuTe (ref. [48]), FeRh (ref. [49]) and Cr_2O_3 (ref. [50]), and stimulated Raman scattering in $KNiF_3$ (ref. [51]). MO effects linear in $\mathbf{L}$ can be observed in AFs for which both time-reversal and space-inversion symmetries are broken. Here, spatial dispersion implies an additional contribution to $\varepsilon^{(s)}_{ij}$ proportional to $\mathbf{k}\cdot\mathbf{L}$, where $\mathbf{k}$ is the light wavevector[52]. Alternatively, light travelling in opposite directions may be transmitted with different intensity and polarization, an effect termed non-reciprocal directional dispersion and demonstrated in CuB_2O_4 (ref. [53]).

Similar MO effects are present also in X-ray[42,54,55] and terahertz[56,57] spectral ranges. For instance, effects quadratic in $\mathbf{L}$ are rather strong in the soft X-ray range due to the resonant enhancement occurring at $2p$ edges of $3d$ transition metals and $3d$ edges of rare-earth elements[42]. Therefore, they enable element-selective

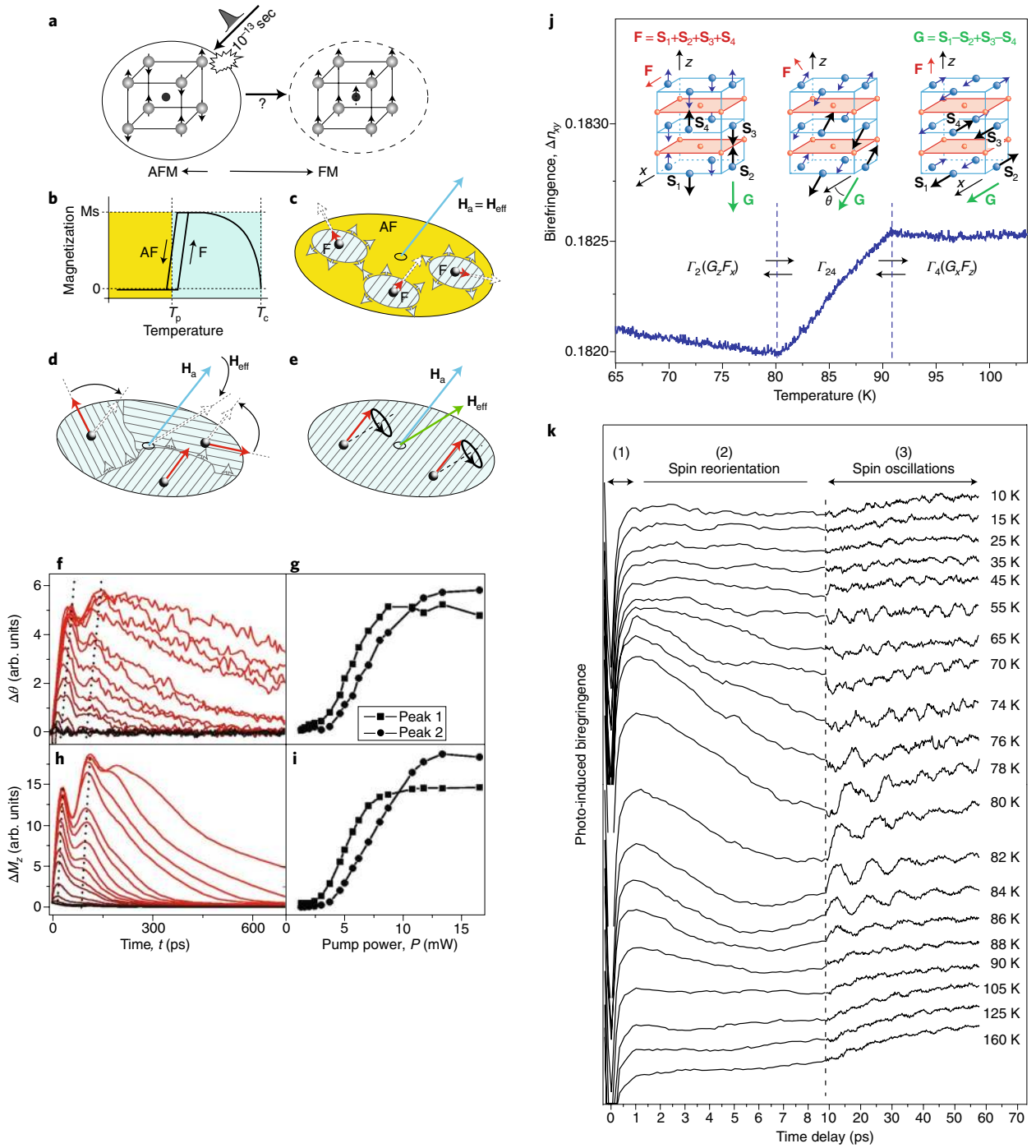

Fig. 4 | Ultrafast modification of magnetic order in FeRh and $TmFeO_3$. **a**, Schematic of the ultrafast generation of ferromagnetic order by inducing an antiferromagnetic-to-ferromagnetic transition in FeRh when excited with femtosecond optical pulses. **b**, At low temperatures, FeRh is antiferromagnetic (yellow) with local iron moments $m_{Fe} = 3\mu_B$ and no appreciable moment on rhodium. At elevated temperatures, the system is ferromagnetic (green) with local iron and rhodium moments of $m_{Fe} \approx 3\mu_B$ and $m_{Fe} \approx 1\mu_B$. **c**, The growth of local magnetization and areal growth of the ferromagnetic phase is followed by a growth of net magnetization by alignment of individual domains. **d**, The demagnetization field grows equally, leading to a canting total effective field. **e**, The homogeneous magnetization starts precessing around the new effective field. The red arrows represent the local magnetization $\mathbf{M}(r,t)$. **f**, Transient Kerr rotation measured at 3.5 kG as a function of time; the applied pump power varies from 1.3 mW (lowest curve) to 16.5 mW (highest curve). **g**, Height of the first and second peaks plotted against the incident pump power. **h**,**i**, Corresponding simulations[94]. **j**, Linear optical birefringence in $TmFeO_3$ as a function of temperature. The insets show the corresponding arrangement of spins: below 80 K the spins lie nearly along the $\pm z$ axes while above 91 K the spins are slightly canted from the $\pm x$ axes. **k**, Excitation and relaxation of the antiferromagnetic moment measured via changes in the magnetic birefringence. When the pump laser pulse is absorbed via the excitation of the localized electronic states of the Fe^{3+} and Tm^{3+} ions, the following relaxation process can be observed. First, the excitation decays via phonon cascades and the phonon system thermalizes with a 0.3-ps relaxation time (process (1)). The phonon–phonon interaction sets a new lattice temperature so that the equilibrium anisotropy axis is changed. Consequently, the resulting motion of spins to the new equilibrium happens with a 5-ps response time (process (2)), which is followed by oscillations of moments around their new equilibrium with an approximate 10-ps period (process (3)). Credit: reproduced from ref. [92], APS (**a**); ref. [94], APS (**b**–**i**); and ref. [33], Macmillan Publishers Ltd (**j**–**k**).

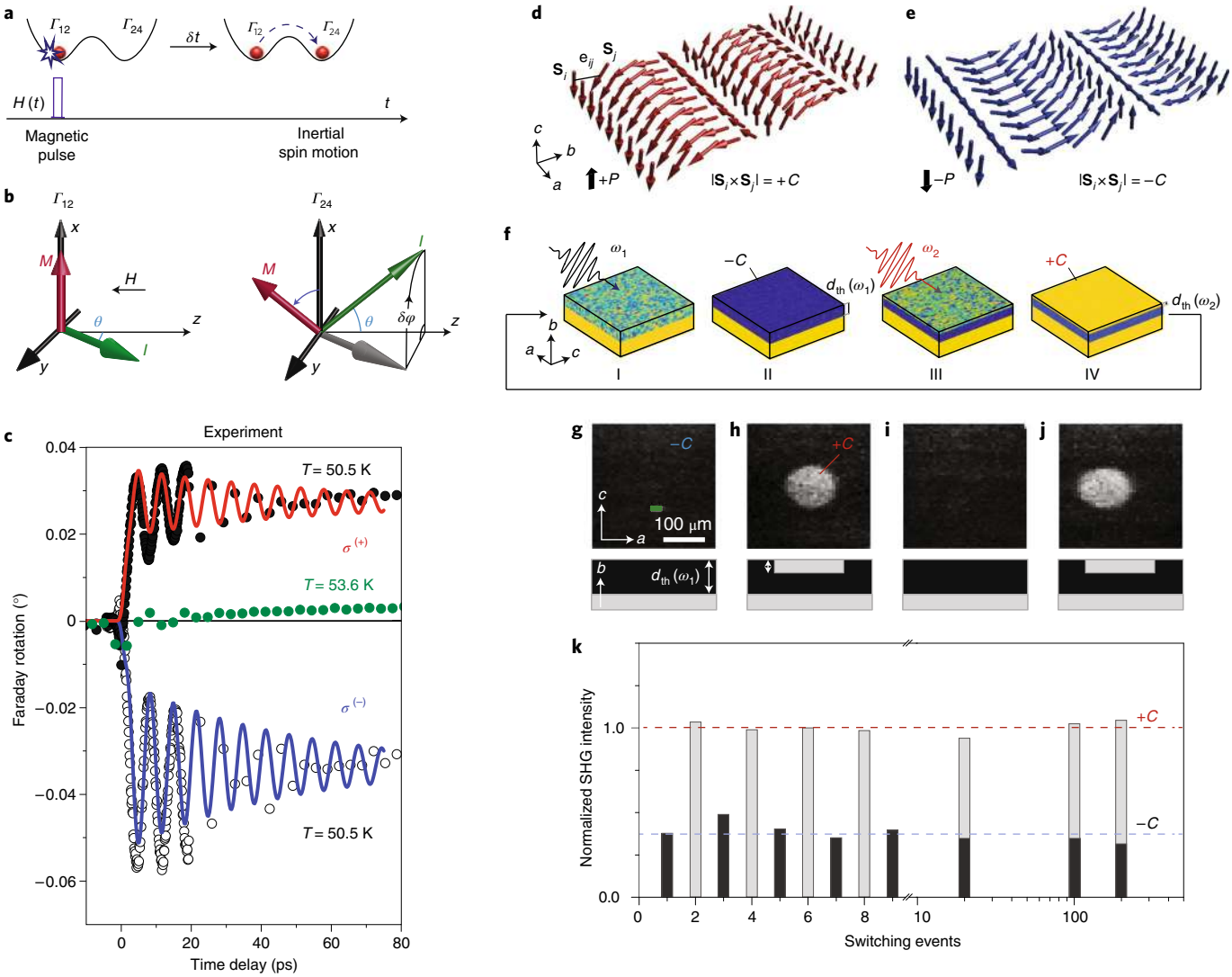

Fig. 5 | Optical switching of the antiferromagnetic state in $HoFeO_3$ and $TbMnO_3$. a, A schematic of the inertial switching between two metastable states. During the action of the driving force, the coordinate of the particle is hardly changed, but the particle acquires enough momentum to overcome the barrier afterwards. **b**, $HoFeO_3$ has two metastable phases, Γ_{12} and Γ_{24}, present between 38 and 52 K. **H** represents an effective magnetic-field pulse with a duration of 100 fs that initiates an inertial motion of spins from the Γ_{12} to the Γ_{24} magnetic phase. In the Γ_{12} phase, the antiferromagnetic vector **L** is in the *yz* plane and the *z* component of magnetization **M** is zero. A transition towards the Γ_{24} phase occurs through a rotation of **L** over an angle $\delta\varphi$ towards the new equilibrium in the *zx* plane with a non-zero M_z component. **c**, The effective magnetic fields along the *z* axis were generated by right-handed (σ^+) and left-handed (σ^-) circularly polarized laser pulses through the inverse Faraday effect in $HoFeO_3$. The trace recorded at T = 53.6 K for a σ^- pump is shown by green points and demonstrates that outside the range 38–52 K no inertia-driven spin switching is seen. **d**,**e**, Antiferromagnetic order in $TbMnO_3$ with spin cycloids of opposite helicity $\pm C$ and associated spin-induced electric polarization $\pm P \propto \pm C$. **f**, Schematics of reversible two-colour switching in $TbMnO_3$. (I) Illumination with ω_1 light heats a region of thickness $d_{th}(\omega_1)$ above the ordering temperature. The underlying bulk remains in the +C state (yellow). (II) After re-cooling, the dipolar stray field exerted by the uniformly polarized environment, which was not photoexcited above T_{AFM} = 27 K, forces the cooling region with a thickness $d_{th}(\omega_1)$ into the opposite polarization state −C state (blue). (III) Illumination with ω_2 light heats a region $d_{th}(\omega_2) < d_{th}(\omega_1)$ above T_0. The intermediate layer remains in the −C state (blue). (IV) Since the intermediate −C layer (blue) screens the stray field of the bulk state (yellow), the $d_{th}(\omega_2)$ top layer reverses to the +C state (yellow). **g**–**k**, Experimental realization of reversible optical switching. **g**, After electric-field cooling to an antiferromagnetic +C state, illumination at ω_1 reverses a top layer to −C. **h**, Local illumination at ω_2 reverses the state to +C. **i**, Illumination at ω_1 recreates the state in **g**. **j**, Repeat of the step in **h**. **k**, Sequential optically induced reversal of the antiferromagnetic state between +C and −C. Columns show the normalized SHG intensity in the area illuminated with light at ω_1 (dark) or ω_2 (bright). Credit: reproduced from ref. [24], Macmillan Publishers Ltd (**a**–**c**); and ref. [5], Macmillan Publishers Ltd (**d**–**k**).

investigations of magnetic materials constituents and element-selective imaging of magnetic domain structures[42,55,58]. Moreover, a combination of X-ray magnetic linear dichroism (XMLD) with photoemission electron microscopy (PEEM) enables direct imaging of antiferromagnetic domains[59–61] with a spatial resolution below 100 nm. This technique was used, for example, for visualization of current-induced changes in the CuMnAs memory device domain structure (see Fig. 2d–j).

For the MO effects described above, the polarization change is independent of the light electric field amplitude **E**, which is a signature of linear optics. However, at high light intensities, nonlinear optical effects appear[62]. In particular, second-harmonic generation

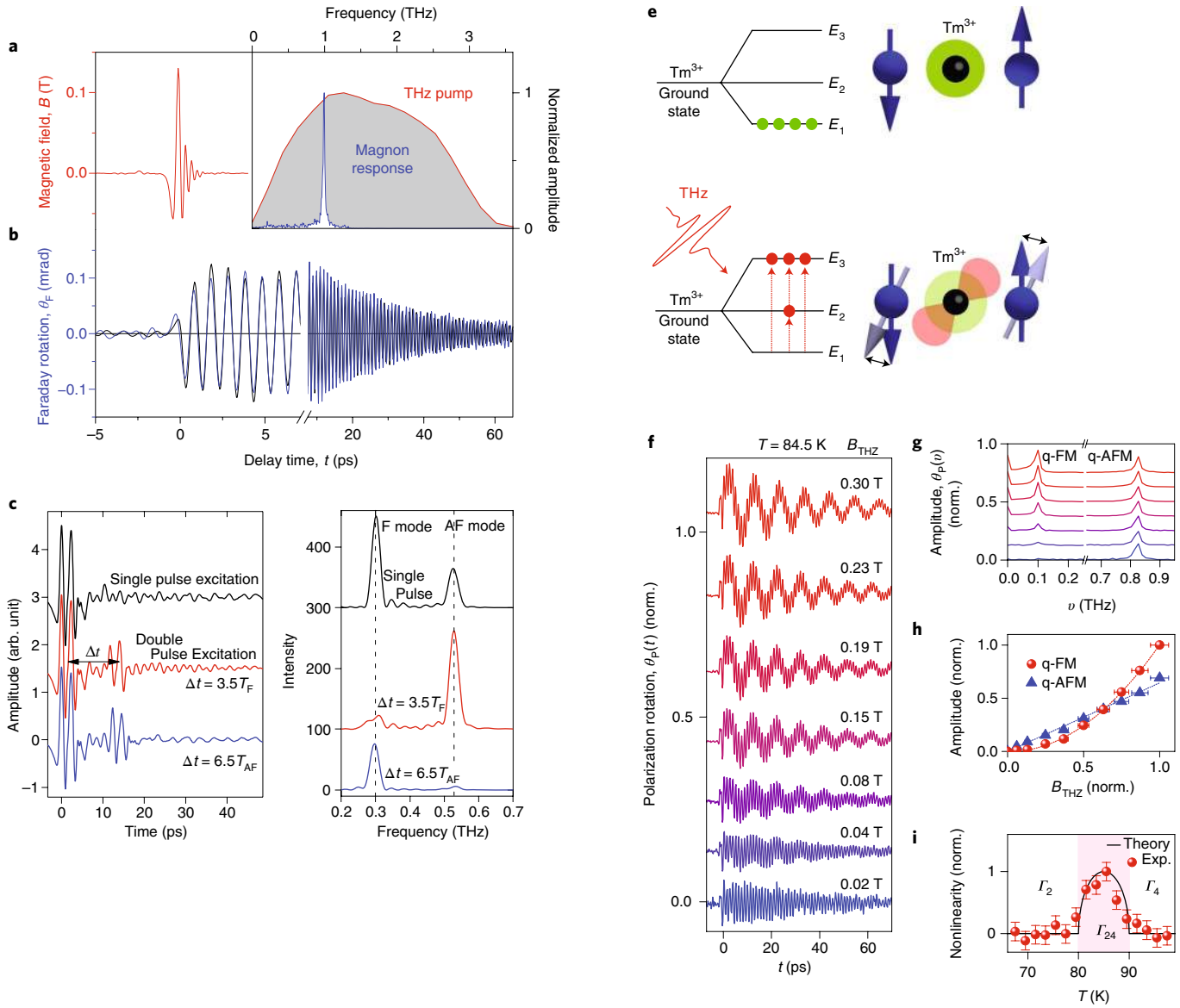

Fig. 6 | Magnetization precession induced by terahertz pulses in NiO, $YFeO_3$ and $TmFeO_3$. **a**, Magnetic field of the incident terahertz pump pulse as a function of time. **b**, Ultrafast Faraday rotation behind the NiO sample (blue curve: experiment; black line: simulation). Harmonic oscillations with a period of 1 ps are due to an antiferromagnetic spin precession. Insets: amplitude spectra of the Faraday transient (**b**) and the driving terahertz field (**a**). **c**, Temporal waveforms of a terahertz pulse transmitted through an *a*-cut plate of $YFeO_3$ for single-pulse and double-pulse excitations. Two pulses are separated in time by time delay Δt; T_F and T_{AF} are the oscillation period of the ferromagnetic and antiferromagnetic mode, respectively. **d**, Spectra obtained by Fourier transformation from 18 to 48 ps in **c**, which shows that the precession modes can be cancelled independently. **e**, The crystal field splits the ground state $^3H_6$ of the rare-earth Tm^{3+} ions into several energy levels with an energy spacing of 1–10 meV (schematic level scheme). The corresponding orbital wavefunctions set the magnetic anisotropy for the Fe^{3+} spins in thermal equilibrium (upper panel). Ultrafast transitions between these energy levels induced by resonant terahertz pulses abruptly modify the magnetic anisotropy and exert torque on the spins, which triggers coherent spin dynamics (lower panel). **f**, Normalized magnon traces measured for various terahertz excitation fields B_{THz} in $TmFeO_3$. While quasi-monochromatic oscillations are found for the lowest terahertz field, a low-frequency oscillation is superimposed onto the dynamics for higher pump fields. **g**, Amplitude spectra of the time-domain data shown in **f** allow the identification of quasi-ferromagnetic (q-FM) and quasi-antiferromagnetic (q-AFM) modes at 100 and 830 GHz, respectively. **h**, Scaling of the amplitudes from **g**. The q-AFM mode scales linearly with the terahertz field strength, whereas the q-FM mode shows a nonlinear dependence. **i**, Deviation of the experimental field-scaling of the q-FM mode with terahertz field strength from a linear behaviour (points) and computed terahertz-induced anisotropy torque exerted on the spins (curve). Credit: reproduced from ref. [20], Macmillan Publishers Ltd (**a**,**b**); ref. [89], APS (**c**,**d**); and ref. [37], Macmillan Publishers Ltd (**e**–**i**).

(SHG), where two photons from the incident wave at frequency ω are annihilated and one photon at frequency 2ω is created, plays a very important role. This effect is described by the expression $\mathbf{P}(2\omega) \propto \mathbf{E}(\omega)\mathbf{E}(\omega)$, and it is restricted to non-centrosymmetric materials[62], but higher-order magnetic-dipole or electric-quadrupole contributions such as $\mathbf{M}(2\omega) \propto \mathbf{E}(\omega)\mathbf{E}(\omega)$ or $\mathbf{P}(2\omega) \propto \mathbf{E}(\omega)\mathbf{H}(\omega)$ may be included in centrosymmetric materials[63,64].

SHG can be used for distinguishing ferroic states on the basis of their different symmetry. For magnetism, this possibility started to be studied theoretically from the 1960s[63,65,66] and experimentally

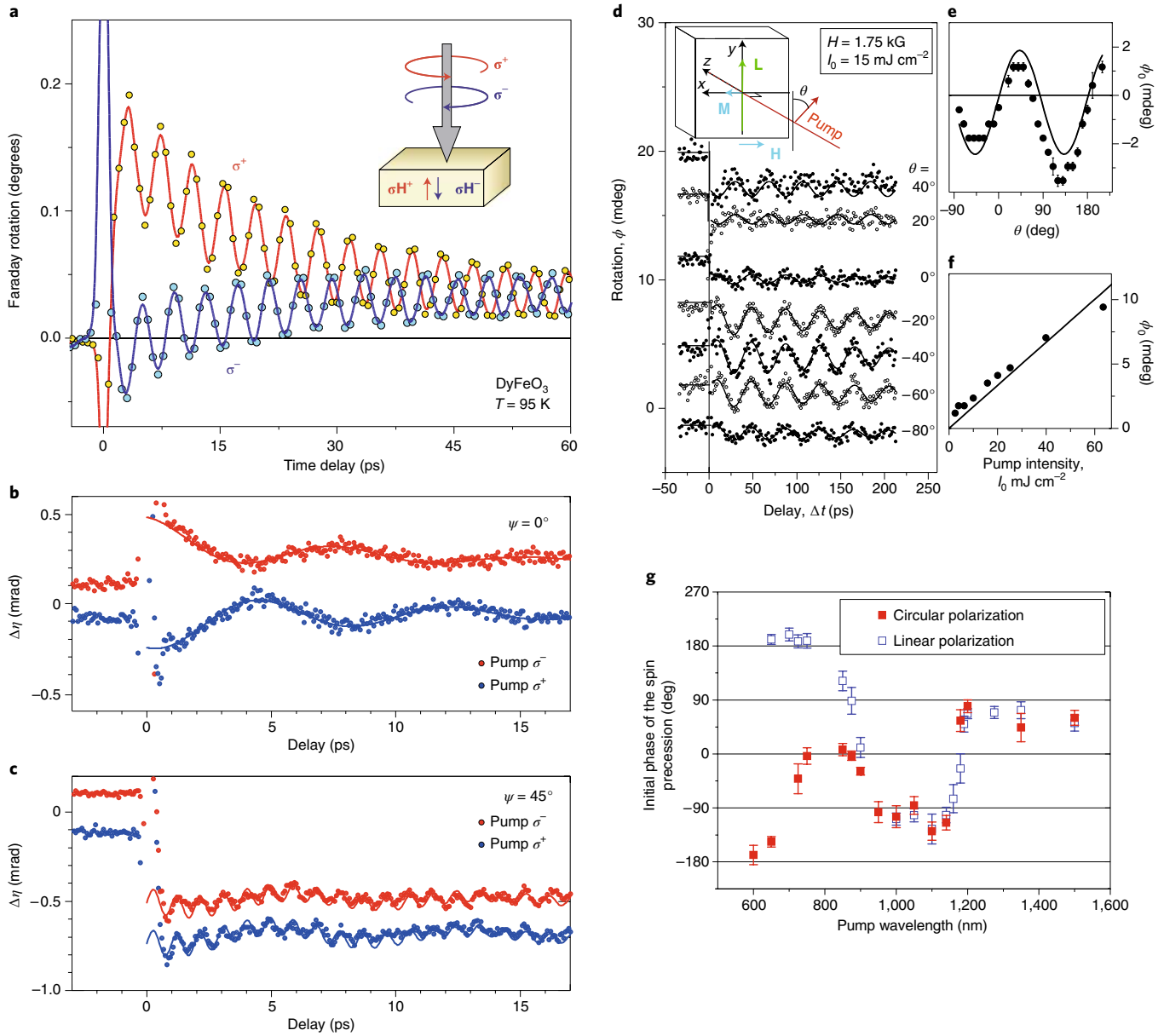

Fig. 7 | Magnetization precession induced by inverse magneto-optical effects in $DyFeO_3$, NiO and $FeBO_3$. **a**, Oscillations of the polarization rotation measured in canted AF $DyFeO_3$ due to precession of Fe spins. The circularly polarized pumps of opposite helicities excite oscillations of opposite phase. Vectors $\delta\mathbf{H}^+$ and $\delta\mathbf{H}^-$ represent the effective magnetic fields induced by right-handed (σ^+) and left-handed (σ^-) circularly polarized pumps, respectively. **b**,**c**, Magnon oscillations in (111)-oriented NiO induced by circularly polarized light and detected by measuring the ellipticity of the probe beam (η). ψ is the angle of the analysed outgoing probe light with respect to the $[11\bar{2}]$ axis. Curves have been displaced by ±0.1 mrad for clarity. In **b**, the signal displays a 180° phase shift following a change in the pump helicity, indicating excitation via the inverse Faraday effect. In **c**, the out-of-plane mode has no pump-helicity dependence, indicating excitation via the inverse Cotton–Mouton effect. **d**, Time-resolved polarization rotation measured in $FeBO_3$ for different linear polarizations of the pump (see inset). **e**,**f**, The oscillation amplitude versus the orientation (**e**) and intensity (**f**) of a linearly polarized pump. **g**, Initial phase of the oscillation as a function of the pump wavelength in $DyFeO_3$. For wavelengths shorter than ≈800 nm, when the phase is a multiple of π, the inverse Faraday effect dominates while for longer wavelengths, when the phase is an odd multiple of π/2, the inverse Cotton–Mouton effect dominates[36]. Credit: reproduced from ref. [34], Macmillan Publishers Ltd (**a**); ref. [19], APS (**b**,**c**); ref. [36], APS (**d**–**f**); and ref. [31], APS (**g**).

from the 1990s[64,67–71]. Nowadays, SHG is a very powerful method that enables one to discriminate magnetic points or even space groups that are indistinguishable to diffraction methods[71]. SHG is especially powerful in the case of AFs (see Fig. 2a–c) where MO effects are usually rather weak, as discussed above. By polarization-dependent SHG spectroscopy, the antiferromagnetic contribution to the SHG intensity can be measured background-free as depicted in Fig. 2b. Using the interference of the signal field with a reference field, it can also be used for a visualization of 180° domains (see Fig. 1a,b) in AFs[5,71,72] (see Fig. 2c). Alternatively, SHG can be employed to probe the pump-induced dynamics in AFs[5,73–75]. Since each form of order breaks symmetry in a different way, magnetic and ferroelectric contributions can be separated via their different polarization and spectral dependences and ordering temperature[71]. Therefore, SHG is ideal for probing the coexistence and coupling of ordered states and domains in multiferroics in a single experiment[76].

Recent advances in terahertz radiation generation motivated a growing interest in this spectral range[77–80]. In contrast to optical radiation, which predominantly interacts with valence electrons,

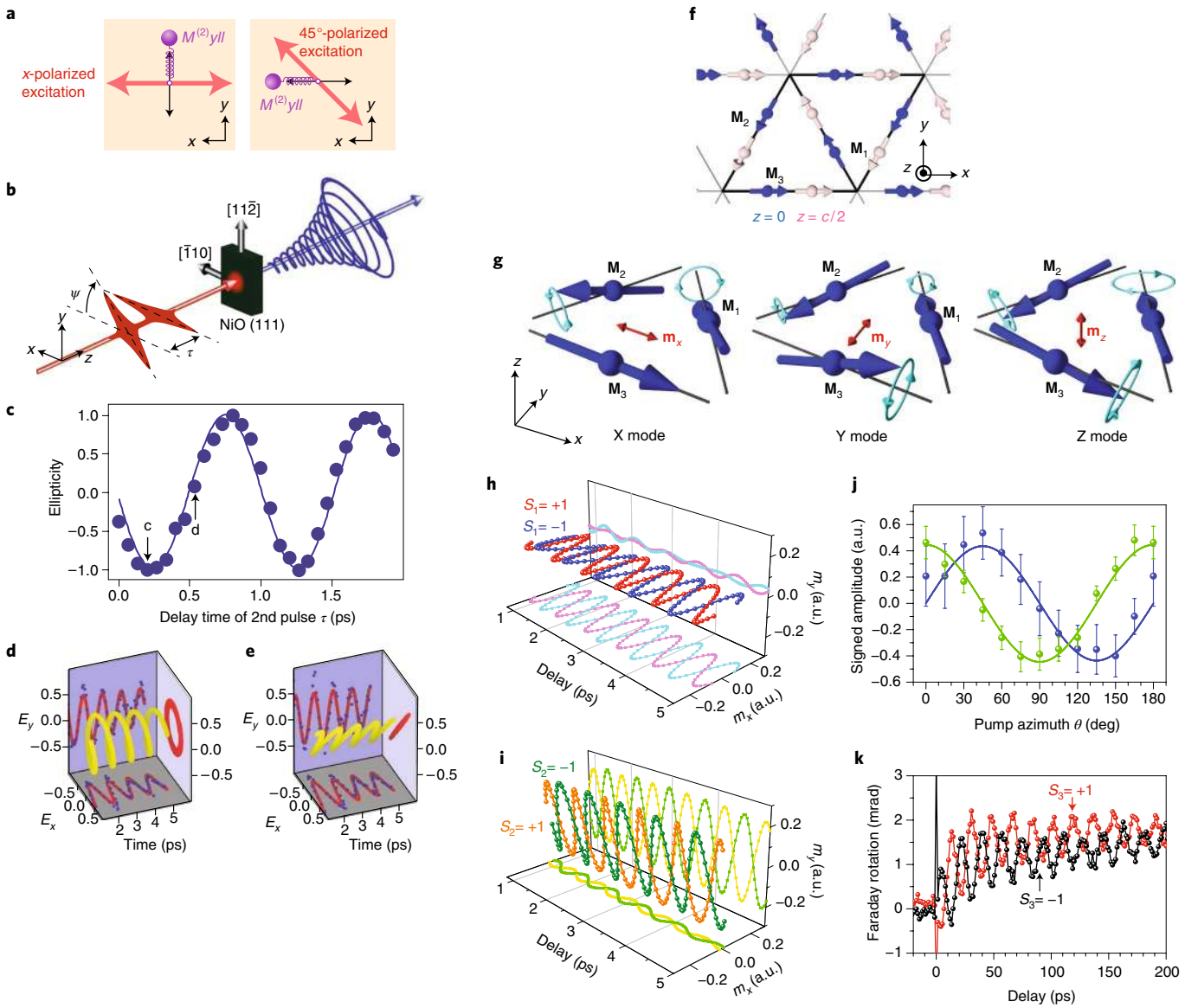

Fig. 8 | Vectorial control of magnetization by light in NiO and $YMnO_3$. **a**, Two orthogonal magnetic oscillation modes in NiO crystal that can be selectively excited by tuning the polarization azimuth of the excitation light pulse. **b**, Schematic illustration of the vectorial control of the magnetization vector with polarization-twisted double-pulse excitation. Both pump pulses are linearly polarized and have a relative time delay τ. The first pulse is polarized along the x axis, whereas the second pulse has an azimuthal angle of ψ. By properly tuning τ and ψ, the motion of the magnetization vector can follow an arbitrarily designed direction and amplitude of polarization. **c**, Ellipticity of the emitted terahertz radiation at the magnon frequency Ω_{mag} as a function of delay τ between the two linearly polarized excitation pulses for $\psi = 45°$. Any ellipticity between the purely right and left circular polarizations is obtained by tuning τ. The solid curve is a fit of the data by a sine curve. **d**,**e**, The three-dimensional trajectories of the electric field vectors with fixed values of τ lead to purely circularly (**d**) and linearly (**e**) polarized radiation. The dots correspond to the projections of the experimental data onto the x and y axes. The solid curves correspond to the fit of exponentially decaying sine functions; the phase differences between the x and y components are determined by $\Omega_{mag}\tau/\pi$. **f**, Antiferromagnetic three-sublattice ordering of the magnetic Mn^{3+} moments in hexagonal $YMnO_3$. **g**, Magnetic oscillation eigenmodes X, Y and Z in $YMnO_3$. **h**, Magnetic 1.3 THz oscillation components excited by a pump pulse with a polarization described by a Stokes parameter $S_1 = \pm 1$ (that is, the pump is linearly polarized along x or y axes, respectively). **i**, The same as **h** for $S_2 = \pm 1$ (that is, the pump is linearly polarized along diagonals ($\boldsymbol{x} + \boldsymbol{y}$) and ($\boldsymbol{x} - \boldsymbol{y}$), respectively). **j**, Signal detected in the X-probe (green) and Y-probe (blue) configurations, as defined in ref. [41], as a function of the angle θ parameterizing the orientation of pump pulse linear polarization. The lines are proportional to cos 2θ (green) and sin 2θ (blue). **k**, Time-dependent Faraday rotation exerted on the probe pulse after excitation by a pump pulse with a polarization described by the Stokes parameter $S_3 = \pm 1$ (that is, the pump is circularly σ^+ or σ^- polarized, respectively). Credit: reproduced from ref. [82], Macmillan Publishers Ltd (**a**–**e**); and ref. [41], Macmillan Publishers Ltd (**f**–**k**).

terahertz radiation couples to low-energy excitations such as molecular rotations, lattice vibrations and spin waves. If magnetization precession is induced (for example, by a laser pulse[18,23,74,75]), the oscillating magnetic dipoles emit an electromagnetic wave (see Fig. 1c). For a thin layer with uniformly oscillating magnetization $\mathbf{M}(t)$ on top of a thick substrate with refractive index n_s, the resulting electric field $\mathbf{E}(t)$ in the air half-space directly behind the magnetic layer can be expressed as[81]

$$\mathbf{E}(t) = \frac{Z_0 n_s d}{(n_s + 1)c} \mathbf{e} \times \frac{\partial \mathbf{M}}{\partial t} \quad (3)$$

Here, $Z_0 \approx 377\,\Omega$ is the vacuum impedance (which is assumed to be much smaller than the magnetic film resistance), and **e** is the unit vector normal to the layer (whose thickness d is assumed to be much smaller than the terahertz wavelength within the layer). As the spin precession frequencies in AFs are as high as several terahertz[18,23,74,75], the emitted radiation with a wavevector **k** is in the terahertz spectral range. Consequently, it is possible to study the projection of the magnetization trajectory on the plane perpendicular to **k** by measuring both linear polarization components of the emitted terahertz wave[82–85]. Therefore, terahertz emission spectroscopy enables one to study ultrafast magnetization dynamics directly. This feature is in contrast to MO[86,87] and SHG[88] experiments where the pump-induced changes in the corresponding coefficients may influence the measured dynamics, especially on subpicosecond timescales. Note that illumination with a resonant terahertz pulse can also induce the spin precession, which can, in turn, be detected by measuring the re-emitted terahertz radiation. This configuration is tantamount to a terahertz transmission experiment and has been routinely applied to characterize long-wavelength antiferromagnetic magnons[89].

Ultrafast modification of magnetic order

Research on ultrafast dynamics of magnetic order is a challenging area in the physics of magnetism. The development of femtosecond lasers has opened the way to create external stimuli that are shorter than fundamental timescales such as spin-lattice relaxation or precession time, thereby allowing for an extremely fast manipulation of the materials magnetic state[18]. As detection of antiferromagnetic order is difficult, these phenomena were originally studied mainly in FMs[18]. Nevertheless, also in AFs there are reports about ultrafast changes of the antiferromagnetic order.

The first prediction of ultrafast antiferromagnetic-order quenching (demagnetization) was reported for NiO[90]. Experimentally, the laser-induced antiferromagnetic-to-paramagnetic state transition was observed in $FeBO_3$ (ref. [32]). Unlike in metallic nickel[91], where the photoexcitation directly heats up the electronic system, the magnetic order quenching in dielectric $FeBO_3$ is caused by an increase in the magnon temperature due to energy transfer from the heated lattice[32]. This phenomenon can also be used for a detailed magnetic characterization of AFs, as demonstrated for a thin film of metal CuMnAs (see Fig. 3).

The dynamic change of magnetic order due to laser excitation was studied in detail in metallic FeRh, which undergoes a first-order magneto-structural transition from an antiferromagnetic to ferromagnetic phase around 380 K (see Fig. 4a). As reported independently in refs [92,93], the illumination of FeRh films by femtosecond laser pulses drives the antiferromagnetic-to-ferromagnetic transformation on a picosecond timescale (see Fig. 4f). Subsequent studies revealed[94,95] that the observed behaviour is due to an interplay between the local magnetic moment, nonlocal domain growth and/or alignment, and magnetization precession (see Fig. 4b–e).

The laser-induced ultrafast reorientation of spins in AF was reported in dielectric $TmFeO_3$ where a temperature-dependent magnetic anisotropy is observed at 80–91 K (see Fig. 4j–k). Similar temperature-related effects were reported for $DyFeO_3$ (ref. [75]) and CuO (ref. [96]). The ultrafast reorientation of Ni^{2+} spins due to the shift of 3d orbital wavefunctions, which accompanies the pump excitation of d–d transitions, was reported in NiO (refs [73,74]). The pump-induced changes of magnetic interactions were studied in detail in AF/FM bilayers (NiO/NiFe (refs [97,98]), FeF_2/Ni (ref. [99]), IrMn/Co (ref. [100]), CoO/Fe (ref. [101]) and CuMnAs/Fe (refs [58,102])).

When the external stimulus (for example, laser pulse) induces a transition between metastable magnetic states, the reorientation of spins leads to spin switching. The fastest way to reorient magnetization in FMs without demagnetization is through precessional motion in an applied field, which can be described by the Landau–Lifshitz–Gilbert equation. This equation is of first order with respect to time, and, therefore, does not contain inertial terms such as acceleration[24]. In other words, the field has to be applied until the magnetization crosses the potential barrier that is separating one minimum from another. In contrast, the dynamics of AFs is described in terms of the motion of the antiferromagnetic unit vector whose equation of motion is of second order with respect to time and, thus, shows inertia-like motion[24] (see Fig. 5a). Consequently, in AFs it is possible to achieve spin switching even if the external stimulus is shorter than the time needed for overcoming the barrier, as demonstrated in $HoFeO_3$ (see Fig. 5b,c). This inertial character of coordinated dynamics of two interacting sublattices is also at the core of the AF switching mechanism by terahertz pulses that was theoretically proposed in ref. [103].

A different approach to achieve reversible optical switching was used in $TbMnO_3$ in ref. [5]. In this material, a helimagnetic spin cycloid with zero net magnetization arises from competing magnetic interactions in the Mn^{3+} sublattice. This induces a ferroelectric polarization, which can be used as a handle to control the antiferromagnetic order (see Fig. 5d–k). Finally, a distinct approach was used in metallic CuMnAs where a reversible switching of antiferromagnetic domains via a spin–orbit torque was induced using a picosecond-long electric field transient in the terahertz range whose polarization direction determined the switched domain orientation[104] (for more details, see the Review by Železný and colleagues[105] in this Focus issue).

Precession of magnetic moments

Antiferromagnetic resonance[35] (that is, generation and detection of spin precession) is an important tool for the development and optimization of antiferromagnetic materials. However, spin precession frequencies in AFs are so high that it is extremely difficult to measure them by common magnetic resonance techniques. For example, for spin waves at the edge of the Brillouin zone of $KNiF_3$, a 20 THz frequency was reported[26]. In the following, we describe several mechanisms that can be used to optically induce magnetic moment precession in AFs. Finally, we show that spin precession in AFs can also be used as a means for information storage.

Conceptually, the most straightforward mechanism is the Zeeman torque between the magnetic field component of an electromagnetic wave and spins. Intense pulses of terahertz radiation with duration shorter than 1 ps and electric- and magnetic-field amplitudes exceeding 1 MVcm^{-1} and 0.33 T, respectively, have recently become available[80]. In Fig. 6, we show experimental data demonstrating this effect in NiO (Fig. 6a,b) and $YFeO_3$ (Fig. 6c,d). Compared to the more common indirect coupling of the light electric field with spins via spin–orbit interaction, the magnetic component of a terahertz pulse exclusively addresses the electron spins and does not deposit excess heat in other degrees of freedom[20]. In addition to Zeeman coupling, intense terahertz electric fields can couple to magnetic excitations nonlinearly through electric-dipole transitions that modify the anisotropy field (see Fig. 6e–i).

As already described, magnetic anisotropy can be modified by the optically induced temperature increase (see Fig. 4j,k). This thermal mechanism was responsible for the precession reported in $TmFeO_3$ (refs [33,35]) and $DyFeO_3$ (ref. [75]). Alternatively, inverse magneto-optical effects can induce the precession in transparent magnetic materials with a strong MO response. In Fig. 7a,b, we show the spin precession induced by the inverse Faraday effect in canted AF $DyFeO_3$ and compensated AF NiO. The fingerprint of this mechanism is a change of the precession phase with the helicity of circularly polarized pump pulses. Microscopically, this effect can be described as optical Stark splitting of spin sublevels or Raman scattering[23,106]. Phenomenologically, it is described in terms of an effective magnetic field pulse, which is present only during the optical pulse (see inset in Fig. 7a), with an amplitude as large as 0.3 T (ref. [34]).

Later it was realized that also linearly polarized laser pulses, even though they do not carry any angular momentum, can generate effective magnetic fields through an inverse Cotton–Mouton effect (see Fig. 7c–f). Here, the fingerprint is the signal harmonic dependence on the linear polarization orientation (see equation (2) and Fig. 7e). The inverse Faraday and Cotton–Mouton effects induce oscillations with a distinct phase that can be used for their experimental separation if they coexist (see Fig. 7b,c,g). Another mechanism that can induce precession of spins in a broad class of iron oxides with canted spin configuration (for example, in $FeBO_3$, $TmFeO_3$, $YFeO_3$ and $ErFeO_3$) is the inverse magneto-refraction. The underlying principle is the exchange interaction modification by the electric field of light, which for laser pulses with fluence of about 1 $mJcm^{-2}$ acts as a pulsed effective magnetic field with a magnitude of 0.01 T (ref. [85]). Similarly, optical modification of the *d–f* exchange interaction between conduction band electrons and lattice spins was shown to trigger spin waves in EuTe (ref. [48]).

Traditionally, optical magnetization control has been limited to a binary process, where light in either of two polarization states writes or reads a magnetic bit carrying either a positive or negative magnetization[105]. However, it is possible to achieve full vectorial control of magnetization by light that can be used for storing multiple pieces of information in a single storage element[41,82]. The implementation requires one to independently address the phase and amplitude of multiple degenerate magnetization modes. This was done in NiO (111), where a micro-multidomain structure with two selectively excited magnetic modes enabled full control of two-dimensional magnetic oscillations with a pair of time-delayed polarization-twisted femtosecond laser pulses (see Fig. 8a–e). Later, this approach was extended to a full three-dimensional control of magnetic oscillations in the three-sublattice antiferromagnet $YMnO_3$ (see Fig. 8f). The idea relies on a one-to-one mapping of the three Stokes parameters, which parameterize the light polarization on the Poincaré sphere, onto three magnetic oscillation modes (see Fig. 8g–k).

Outlook

As we have seen, antiferromagnetic states and interactions, which have for a long time eluded convenient detection and manipulation, are now becoming more and more accessible. In particular, swift feedback loops between manipulation of an antiferromagnetic state and observation of the consequences of this manipulation were established. These powerful optical tools will speed up progress in the field of antiferromagnetic engineering considerably. We, therefore, believe that antiferro-magneto-optics is the realm where the biggest advances in antiferromagnetic opto-spintronics will occur in the near future.

Research on new MO effects for observation will most likely focus on systems with complex antiferromagnetic states, because only they provide order parameters of a complexity that makes new or exotic phenomena symmetry-allowed. Examples are non-collinear spin structures, spin spirals, multiply magnetically ordered compounds, magnetic ferroelectrics (multiferroics) or topological magnetic states (such as skyrmions). Studying their MO properties is facilitated by the fact that solid-state properties of these systems are relatively well explored. On the other hand, complexity can be tailored with heterostructures involving antiferromagnetic constituents or interfaces, or by designing mesoscale systems with antiferromagnetic building blocks. The challenge of manufacturing such structurally advanced systems is met by the recent tremendous advances in oxide-electronics growth techniques. Examples for MO effects that can arise in such architectures are non-reciprocal directional dichroism up to the point of one-way optical transparency and nonlinear optical effects with much larger relative strength than their linear counterparts. New MO phenomena in AFs can also extend into other frequency ranges. The recent developments of free-electron and table-top lasers operating in the extreme ultraviolet and X-ray spectral ranges are expected to facilitate new breakthroughs in understanding the physics of AFs. At the low-frequency side, terahertz radiation can excite electromagnons as dynamic mixed antiferromagnetic–dielectric states.

Investigation of new MO effects for manipulation should focus on ultrafast phenomena. Whereas 20 years of research have been spent on ultrafast magnetization dynamics in FMs, that in AFs has received far less attention. Nevertheless, their research has already revealed phenomena exclusively possible in AFs, which include the inherently higher speed and the presence of inertia. It is also expected that the boosting field of all-optical recording will be expanded from ferro- and ferrimagnets to AFs. For multiferroics, which are mostly AFs, dynamical phenomena are still a highly underrated topic. Even though the magnetoelectric switching is one of the declared goals of the field, hardly any attention has been paid to the temporal evolution of the order parameter reversal or the corresponding domain pattern evolution. Recently demonstrated possibilities of spin control using both electric and magnetic components of light open up intriguing opportunities for the implementation of coherent (quantum) control in AFs by interference between these two channels. Direct pumping of spin excitations in AFs with the help of a freely propagating terahertz wave suggests that the wave is strongly coupled to the excitations in the medium and, therefore, propagates as a polariton. The physics of magnon–polaritons at terahertz frequencies has obtained hardly any attention so far and calls for interdisciplinary research at the intersection of magnetism and photonics. Many other concepts of spintronics and magnonics are yet to be demonstrated for AFs, among which investigation of the spatial and temporal evolution of spin pumping from AFs is one of the next challenges. Overall, the research in the field of antiferromagnetic opto-spintronics is just beginning.

Received: 30 May 2017; Accepted: 17 January 2018;
Published online: 2 March 2018

References

1. Néel, L. Propriétées magnétiques des ferrites; férrimagnétisme et antiferromagnétisme. *Ann. Phys. (Paris)* **3**, 137–198 (1948).
2. Dzyaloshinsky, I. A thermodynamic theory of "weak" ferromagnetism of antiferromagnetics. *J. Phys. Chem. Solids* **4**, 241–255 (1958).
3. Moriya, T. Anisotropic superexchange interaction and weak ferromagnetism. *Phys. Rev.* **120**, 91–98 (1960).
4. Fiebig, M., Lottermoser, Th, Meier, D. & Trassin, M. The evolution of multiferroics. *Nat. Rev. Mater.* **1**, 16046 (2016).
5. Manz, S. et al. Reversible optical switching of antiferromagnetism in $TbMnO_3$. *Nat. Photon.* **10**, 653–656 (2016).
6. Duine, R. A., Lee, K.-J., Parkin, S. S. P. & Stiles, M. D. Synthetic antiferromagnetic spintronics. *Nat. Phys.* https://doi.org/s41567-018-0050-y (2018).
7. Stiles, M. D. in *Ultrathin Magnetic Structures III, Fundamentals of Nanomagnetism* (eds Bland, J. A. C. & Heinrich, B.) Ch. 4 (Springer, Berlin, 2005).
8. Shick, A. B., Khmelevskyi, S., Mryasov, O. N., Wunderlich, J. & Jungwirth, T. Spin–orbit coupling induced anisotropy effects in bimetallic antiferromagnets: A route towards antiferromagnetic spintronics. *Phys. Rev. B* **81**, 212409 (2010).
9. MacDonald, A. H. & Tsoi, M. Antiferromagnetic metal spintronics. *Phil. Trans. R. Soc. A* **369**, 3098–3114 (2011).
10. Gomonay, E. V. & Loktev, V. M. Spintronics of antiferromagnetic systems. *Low Temp. Phys.* **40**, 17–35 (2014).
11. Jungwirth, T., Marti, X., Wadley, P. & Wunderlich, J. Antiferromagnetic spintronics. *Nat. Nanotech.* **11**, 231–241 (2016).
12. Gomonay, O., Jungwirth, T. & Sinova, J. Concepts of antiferromagnetic spintronics. *Phys. Stat. Sol. RRL.* **11**, 1700022 (2017).
13. Baltz, V. et al. Antiferromagnetic spintronics. *Rev. Mos. Phys.* **90**, 015005 (2018).
14. Marti, X. et al. Room-temperature antiferromagnetic memory resistor. *Nat. Mater.* **13**, 367–374 (2014).
15. Wadley, P. et al. Electrical switching of an antiferromagnet. *Science* **351**, 587–590 (2016).
16. Kriegner, D. et al. Multiple-stable anisotropic magnetoresistance memory in antiferromagnetic MnTe. *Nat. Commun.* **7**, 11623 (2016).

17. Olejník, K. et al. Antiferromagnetic CuMnAs multi-level memory cell with microelectronic compatibility. *Nat. Commun.* **8**, 15434 (2017).
18. Kirilyuk, A., Kimel, A. V. & Rasing, Th. Ultrafast optical manipulation of magnetic order. *Rev. Mod. Phys.* **82**, 2731–2784 (2010).
19. Tzschaschel, C. et al. Ultrafast optical excitation of coherent magnons in antiferromagnetic NiO. *Phys. Rev. B* **95**, 174407 (2017).
20. Kampfrath, T. et al. Coherent terahertz control of antiferromagnetic spin waves. *Nat. Photon.* **5**, 31–34 (2011).
21. Pashkin, A., Sell, A., Kampfrath, T. & Huber, R. Electric and magnetic terahertz nonlinearities resolved on the sub-cycle scale. *New J. Phys.* **15**, 065003 (2013).
22. Zvezdin, A. K. & Kotov, V. A. *Modern Magnetooptics and Magnetooptical Materials* (Institute of Physics Publishing, Bristol, 1997).
23. Ivanov, B. A. Spin dynamics of antiferromagnets under action of femtosecond laser pulses. *Low Temp. Phys.* **40**, 91–105 (2014).
24. Kimel, A. V. et al. Inertia-driven spin switching in antiferromagnets. *Nat. Phys.* **5**, 727–731 (2009).
25. Bossini, D., Kalashnikova, A. M., Pisarev, R. V., Rasing, Th & Kimel, A. V. Controlling coherent and incoherent spin dynamics by steering the photoinduced energy flow. *Phys. Rev. B* **89**, 060405 (2014).
26. Bossini, D. et al. Macrospin dynamics in antiferromagnets triggered by sub-20 femtosecond injection of nanomagnons. *Nat. Commun.* **7**, 10645 (2016).
27. Zhao, J., Bragas, A. V., Lockwood, D. J. & Merlin, R. Magnon squeezing in an antiferromagnet: reducing the spin noise below the standard quantum limit. *Phys. Rev. Lett.* **93**, 107203 (2004).
28. Ferre, J. & Gehring, G. A. Linear optical birefringence of magnetic crystals. *Rep. Prog. Phys.* **47**, 513–611 (1984).
29. McCord, J. Progress in magnetic domain observation by advanced magneto-optical microscopy. *J. Phys. D* **48**, 333001 (2015).
30. Smolenskiĭ, G. A., Pisarev, R. V. & Siniĭ, I. G. Birefringence of light in magnetically ordered crystals. *Sov. Phys. Usp.* **18**, 410–429 (1975).
31. Iida, R. et al. Spectral dependence of photoinduced spin precession in $DyFeO_3$. *Phys. Rev. B.* **84**, 064402 (2011).
32. Kimel, A. V., Pisarev, R. V., Hohlfeld, J. & Rasing, Th Ultrafast quenching of the antiferromagnetic order in $FeBO_3$: direct optical probing of the phonon–magnon coupling. *Phys. Rev. Lett.* **89**, 287401 (2002).
33. Kimel, A. V., Kirilyuk, A., Tsvetkov, A., Pisarev, R. V. & Rasing, Th Laser-induced ultrafast spin reorientation in the antiferromagnet $TmFeO_3$. *Nature* **429**, 850–853 (2004).
34. Kimel, A. V. et al. Ultrafast non-thermal control of magnetization by instantaneous photomagnetic pulses. *Nature* **435**, 655–657 (2005).
35. Kimel, A. V. et al. Optical excitation of antiferromagnetic resonance in $TmFeO_3$. *Phys. Rev. B* **74**, 060403(R) (2006).
36. Kalashnikova, A. M. et al. Impulsive generation of coherent magnons by linearly polarized light in the easy-plane antiferromagnet $FeBO_3$. *Phys. Rev. Lett.* **99**, 167205 (2007).
37. Baierl, S. et al. Nonlinear spin control by terahertz-driven anisotropy fields. *Nat. Photon.* **10**, 715–718 (2016).
38. Feng, W., Guo, G.-Y., Zhou, J., Yao, Y. & Niu, Q. Large magneto-optical Kerr effect in noncollinear antiferromagnets Mn_3X (X = Rh, Ir, Pt). *Phys. Rev. B* **92**, 144426 (2015).
39. Eremenko, V. V., Kharchenko, N. F., Litvinenko, Y. G. & Naumenko, V. M. *Magneto-Optics and Spectroscopy of Antiferromagnets* (Springer-Verlag, New York, NY, 1992).
40. Andreev, A. F. & Marchenko, V. I. Symmetry and the macroscopic dynamics of magnetic materials. *Sov. Phys. Usp.* **23**, 21–34 (1980).
41. Satoh, T., Iida, R., Higuchi, T., Fiebig, M. & Shimura, T. Writing and reading of an arbitrary optical polarization state in an antiferromagnet. *Nat. Photon.* **9**, 25–29 (2015).
42. Mertins, H.-C. et al. Magneto-optical polarization spectroscopy with soft X-rays. *Appl. Phys. A* **80**, 1011–1020 (2005).
43. Tesařová, N. et al. Direct measurement of the three-dimensional magnetization vector trajectory in GaMnAs by a magneto-optical pump-and-probe method. *Appl. Phys. Lett.* **100**, 102403 (2012).
44. Tesařová, N. et al. Systematic study of magnetic linear dichroism and birefringence in (Ga,Mn)As. *Phys. Rev. B* **89**, 085203 (2014).
45. Saidl, V. et al. Optical determination of the Néel vector in a CuMnAs thin-film antiferromagnet. *Nat. Photon.* **11**, 91–97 (2017).
46. Tesarova, N. et al. High precision magnetic linear dichroism measurements in (Ga,Mn)As. *Rev. Sci. Instrum.* **83**, 123108 (2012).
47. Ehrke, H. et al. Photoinduced melting of antiferromagnetic order in $La_{0.5}Sr_{1.5}MnO_4$ measured using ultrafast resonant soft X-ray diffraction. *Phys. Rev. Lett.* **106**, 217401 (2011).
48. Subkhangulov, R. R. et al. All-optical manipulation and probing of the d–f exchange interaction in EuTe. *Sci. Rep.* **4**, 4368 (2014).
49. Saidl, V. et al. Investigation of magneto-structural phase transition in FeRh by reflectivity and transmittance measurements in visible and near-infrared spectral region. *New J. Phys.* **18**, 083017 (2016).
50. Dodge, J. S., Schumacher, A. B., Bigot, J.-Y. & Chemla, D. S. Time-resolved optical observation of spin-wave dynamics. *Phys. Rev. Lett.* **83**, 4650–4653 (1999).
51. Batignani, G. et al. Probing ultrafast photo-induced dynamics of the exchange energy in a Heisenberg antiferromagnet. *Nat. Photon.* **9**, 506–510 (2015).
52. Krichevstov, B. B., Pavlov, V. V., Pisarev, R. V. & Gridnev, V. N. Spontaneous nonreciprocal reflection of light from antiferromagnetic Cr_2O_3. *J. Phys. Cond. Mat.* **5**, 8233–8244 (1993).
53. Toyoda, S. et al. One-way transparency of light in multiferroic CuB_2O_4. *Phys. Rev. Lett.* **115**, 267207 (2015).
54. Valencia, S. et al. Quadratic X-ray magneto-optical effect upon reflection in a near-normal-incidence configuration at the *M* edges of 3*d*-transition metals. *Phys. Rev. Lett.* **104**, 187401 (2010).
55. Wadley, P. et al. Antiferromagnetic structure in tetragonal CuMnAs thin films. *Sci. Rep.* **5**, 17079 (2015).
56. Shimano, R. et al. Terahertz Faraday rotation induced by an anomalous Hall effect in the itinerant ferromagnet $SrRuO_3$. *Eur. Phys. Lett.* **95**, 17002 (2011).
57. Huisman, T. J. et al. Terahertz magneto-optics in the ferromagnetic semiconductor $HgCdCr_2Se_4$. *Appl. Phys. Lett.* **106**, 132411 (2015).
58. Wadley, P. et al. Control of antiferromagnetic spin axis orientation in bilayer Fe/CuMnAs films. *Sci. Rep.* **7**, 11147 (2017).
59. Scholl, A. et al. Observation of antiferromagnetic domains in epitaxial thin films. *Science* **287**, 1014–1016 (2000).
60. Nolting, F. et al. Direct observation of the alignment of ferromagnetic spins by antiferromagnetic spins. *Nature* **405**, 767–769 (2000).
61. Grzybowski, M. J. et al. Imaging current-induced switching of antiferromagnetic domains in CuMnAs. *Phys. Rev. Lett.* **118**, 057701 (2017).
62. Boyd, R. W. *Nonlinear Optics* (Elsevier, Amsterdam, 2008).
63. Pershan, P. S. Nonlinear optical properties of solids: energy considerations. *Phys. Rev.* **130**, 919–929 (1963).
64. Fiebig, M., Fröhlich, D., Krichevtsov, B. B. & Pisarev, R. V. Second harmonic generation and magnetic-dipole-electric-dipole interference in antiferromagnetic Cr_2O_3. *Phys. Rev. Lett.* **73**, 2127–2130 (1994).
65. Adler, E. Nonlinear optical frequency polarization in a dielectric. *Phys. Rev.* **134**, A728–A733 (1964).
66. Lajzerowicz, J. & Vallade, M. Génération du second harmonique dans les substances magnétiques ordonnées. *C. R. Seances Acad. Sci. B* **264**, 1819–1821 (1967).
67. Agaltsov, A. M., Gorelik, V. S., Zvezdin, A. K., Murashov, V. A. & Rakov, D. N. Temperature dependence of the second harmonic generation in ferroelectric-magnetic bismuth ferrite. *Sov. Phys. Short Commun.* **5**, 37–39 (1989).
68. Reif, J., Zink, J. C., Schneider, C.-M. & Kirschner, J. Effects of surface magnetism on optical second harmonic generation. *Phys. Rev. Lett.* **67**, 2878–2881 (1991).
69. Reif, J., Rau, C. & Matthias, E. Influence of magnetism on second harmonic generation. *Phys. Rev. Lett.* **71**, 1931–1934 (1993).
70. Murashov, V. A. et al. Magnetoelectric (Bi, Ln)FeO_3 compounds: crystal growth, structure and properties. *Ferroelectrics* **162**, 11–21 (1994).
71. Fiebig, M., Pavlov, V. V. & Pisarev, R. V. Second-harmonic generation as a tool for studying electronic and magnetic structures of crystals. *J. Opt. Soc. Am. B* **22**, 96–118 (2005).
72. Fiebig, M., Fröhlich, D., Lottermoser, T. & Kallenbach, S. Phase-resolved second-harmonic imaging with non-ideal laser sources. *Opt. Lett.* **29**, 41–43 (2004).
73. Duong, N. P., Satoh, T. & Fiebig, M. Ultrafast manipulation of antiferromagnetism of NiO. *Phys. Rev. Lett.* **93**, 117402 (2004).
74. Rubano, A. et al. Influence of laser pulse shaping on the ultrafast dynamics in antiferromagnetic NiO. *Phys. Rev. B* **82**, 174431 (2010).
75. Afanasiev, D. et al. Control of the ultrafast photoinduced magnetization across the morin transition in $DyFeO_3$. *Phys. Rev. Lett.* **16**, 097401 (2016).
76. Fiebig, M., Lottermoser, Th, Fröhlich, D., Goltsev, A. V. & Pisarev, R. V. Observation of coupled magnetic and electric domains. *Nature* **419**, 818–820 (2002).
77. Tonouchi, M. Cutting-edge terahertz technology. *Nat. Photon.* **1**, 97–105 (2007).
78. Ulbricht, R., Hendry, E., Shan, J., Heinz, T. F. & Bonn, M. Carrier dynamics in semiconductors studied with time-resolved terahertz spectroscopy. *Rev. Mod. Phys.* **83**, 543–586 (2011).
79. Hoffmann, M. C. in *Terahertz Spectroscopy and Imaging* (eds Peiponen, K.-E., Zeitler, A. & Kuwata-Gonokami, M.) Ch. 14 (Springer, Berlin, 2013).
80. Kampfrath, T., Tanaka, K. & Nelson, K. A. Resonant and nonresonant control over matter and light by intense terahertz transients. *Nat. Photon.* **7**, 680–690 (2013).
81. Kampfrath, T. et al. Terahertz spin current pulses controlled by magnetic heterostructures. *Nat. Nanotech.* **8**, 256–260 (2013).
82. Kanda, N. et al. The vectorial control of magnetization by light. *Nat. Commun.* **2**, 362 (2011).

83. Nishitani, J., Kozuki, K., Nagashima, T. & Hangyo, M. Terahertz radiation from coherent antiferromagnetic magnons excited by femtosecond laser pulses. *Appl. Phys. Lett.* **96**, 221906 (2010).
84. Nishitani, J., Nagashima, T. & Hangyo, M. Coherent control of terahertz radiation from antiferromagnetic magnons in NiO excited by optical laser pulses. *Phys. Rev. B* **85**, 174439 (2012).
85. Mikhaylovskiy, R. V. Terahertz magnetization dynamics induced by femtosecond resonant pumping of Dy^{3+} subsystem in the multisublattice antiferromagnet $DyFeO_3$. *Phys. Rev. B* **92**, 094437 (2015).
86. Koopmans, B., van Kampen, M., Kohlhepp, J. T. & de Jonge, W. J. M. Ultrafast magneto-optics in nickel: magnetism or optics? *Phys. Rev. Lett.* **85**, 844–847 (2000).
87. Kampfrath, T. et al. Ultrafast magneto-optical response of iron thin films. *Phys. Rev. B* **65**, 104429 (2002).
88. Regensburger, H., Vollmer, R. & Kirschner, J. Time-resolved magnetization-induced second-harmonic generation from the Ni(110) surface. *Phys. Rev. B* **61**, 14716 (2000).
89. Yamaguchi, K., Nakajima, M. & Suemoto, T. Coherent control of spin precession motion with impulsive magnetic fields of half-cycle terahertz radiation. *Phys. Rev. Lett.* **105**, 237201 (2010).
90. Ney, O., Trzeciecki, M. & Huebner, W. Femtosecond dynamics of spin-dependent SHG response from NiO (001). *Appl. Phys. B* **74**, 741–744 (2002).
91. Beaurepaire, E., Merle, J.-C., Daunois, A. & Bigot, J.-Y. Ultrafast spin dynamics in ferromagnetic nickel. *Phys. Rev. Lett.* **76**, 4250 (1996).
92. Ju, G. et al. Ultrafast generation of ferromagnetic order via a laser-induced phase transformation in FeRh thin films. *Phys. Rev. Lett.* **93**, 197403 (2004).
93. Thiele, J.-U., Buess, M. & Back, C. H. Spin dynamics of the antiferromagnetic-to-ferromagnetic phase transition in FeRh on a sub-picosecond time scale. *Appl. Phys. Lett.* **85**, 2857–2859 (2004).
94. Bergman, B. et al. Identifying growth mechanisms for laser-induced magnetization in FeRh. *Phys. Rev. B* **73**, 060407(R) (2006).
95. Mariager, S. O. et al. Structural and magnetic dynamics of a laser induced phase transition in FeRh. *Phys. Rev. Lett.* **108**, 087201 (2012).
96. Johnson, S. L. et al. Femtosecond dynamics of the collinear-to-spiral antiferromagnetic phase transition in CuO. *Phys. Rev. Lett.* **108**, 037203 (2012).
97. Ju, G. et al. Ultrafast time resolved photoinduced magnetization rotation in a ferromagnetic/antiferromagnetic exchange coupled system. *Phys. Rev. Lett.* **82**, 3705–3708 (1999).
98. McCord, J., Kaltofen, R., Gemming, T., Hühne, R. & Schultz, L. Aspects of static and dynamic magnetic anisotropy in $Ni_{81}Fe_{19}$-NiO films. *Phys. Rev. B* **75**, 134418 (2007).
99. Porat, A., Bar-Ad, S. & Schuller, I. K. Novel laser-induced dynamics in exchange-biased systems. *Eur. Phys. Lett.* **87**, 67001 (2009).
100. Longa, F. D., Kohlhepp, J. T., de Jonge, W. J. M. & Koopmans, B. Resolving the genuine laser-induced ultrafast dynamics of exchange interaction in ferromagnet/antiferromagnet bilayers. *Phys. Rev. B* **81**, 094435 (2010).
101. Ma, X. et al. Ultrafast spin exchange-coupling torque via photo-excited charge-transfer processes. *Nat. Commun.* **6**, 8800 (2015).
102. Saidl, V. et al. Investigation of exchange coupled bilayer Fe/CuMnAs by pump-probe experiment. *Phys. Stat. Sol. RRL* **11**, 1600441 (2017).
103. Wienholdt, S., Hinzke, D. & Nowak, U. THz switching of antiferromagnets and ferrimagnets. *Phys. Rev. Lett.* **108**, 247207 (2012).
104. Olejník, K et al. THz electrical writing speed in an antiferromagnetic memory. *Sci. Adv.* (in the press); preprint at https://arxiv.org/abs/1711.08444
105. Železný, J., Wadley, P., Olejník, K., Hoffmann, A. & Ohno, H. Spin-transport and spin-torque in antiferromagnetic devices. *Nat. Phys.* https://doi.org/s41567-018-0062-7 (2018).
106. Battiato, M., Barbalinardo, G. & Oppeneer, P. M. Quantum theory of the inverse Faraday effect. *Phys. Rev. B* **89**, 014413 (2014).
107. Stupakiewicz, A., Szerenos, K., Afanasiev, D., Kirilyuk, A. & Kimel, A. V. Ultrafast nonthermal photo-magnetic recording in a transparent medium. *Nature* **542**, 71–79 (2017).

Acknowledgements

P.N. acknowledges support from the Grant Agency of the Czech Republic under grant no. 14-37427G, the Ministry of Education of the Czech Republic under grants LM2015087 and LNSM-LNSpin, and the EU FET Open RIA grant no. 766566. A.V.K. acknowledges the Netherlands Foundation of Scientific Research (NWO) and the Ministry of Education and Science of the Russian Federation (project no. 14.Z50.31.0034). T.K. thanks the European Research Council for support through grant no. 681917 (TERAMAG) and the German Research Foundation through CRC/TRR 227. M.F. acknowledges support from the SNSF project 200021/147080 and by FAST, a division of the SNSF NCCR MUST.

Additional information